JOURNAL OF MATERIALS SCIENCE 23 (1988) 2931–2942

Microstructure and scaling effects in the damage of WC–Co alloys by single impacts of hard particles

K. ANAND, H. CONRAD
Materials Science and Engineering Department, North Carolina Sate University, Raleigh, North Carolina 27695-7907, USA

The size and nature of the craters produced by single impacts of angular Al_2O_3 particles on WC–Co alloys (6 to 50 wt% Co) were investigated as a function of microstructure, impacting particle size (63 to 405 μm), velocity (35 to 93 m sec^{-1}) and angle of impact (30 to 90°). In general, the size of the craters increased with increase in particle size and velocity and with cobalt content of the target. Two distinct types of behaviour occurred depending on the number of WC grains encompassed by the projected area of the crater. When the number was less than 10, the crater was formed mainly by cracking of WC grains (brittle regime); when it was more than 100, the crater resulted mainly from the plastic deformation of the binder phase (ductile regime). The cracking of the WC grains in the brittle regime did not have the typical appearance of either cone or lateral cracks. The behaviour in the ductile regime correlated reasonably well with the model for plastic indentation; the derived work of plastic deformation was, however, only about 10% of the initial kinetic energy of the impacting particle. Besides the usual elastic effects, fragmentation of particles was considered to be responsible for a significant fraction of the kinetic energy loss, The effects of microstructure of the target on the crater size in the ductile regime was deduced to be mainly through its effect on the hardness, which was given reasonably well by the Lee and Gurland relation.

1. Introduction

Because of their high hardness combined with some ductility, cemented carbides find application where resistance to wear and/or erosion is an important consideration. Studies on the erosion of WC–Co alloys by hard particles [1–5] show that depending on the erosion conditions the behaviour may change from one characteristic of a brittle material, where the maximum erosion rate occurs at normal impact, to one resembling a ductile material, where maximum erosion rate occurs at an oblique angle [6]. The brittle signature in WC–Co alloys was favoured by a larger WC grain size and less severe erosion conditions (smaller impacting particle size and/or velocity), whereas the ductile signature was favoured by the more severe erosion conditions and smaller WC grain size. By independently altering the severity of the erosion conditions or the WC grain size, the erosion character for a given WC–Co alloy could be changed from the brittle to the ductile type, or vice versa [5]. The interchangeability between the severity of the erosion conditions and the WC grain size suggests an influence of scaling between the impact damage zone size and the microstructure of the WC–Co alloy. Scaling effects have also been noted in microscopy studies of the erosion damage of a number of metal and ceramic systems [7–10]. However, up to now no detailed quantitative study has been made on the effects of scaling between the impact damage zone size and the microstructure size. The objective of the present investigation was, therefore, to determine the effects of impact conditions and microstructure on the size of the craters produced by single impacts of hard angular particles on WC–Co alloys and, in turn, the effects of scaling on the size and nature of the resulting damage. To this end, the size of the microconstituents of the WC–Co alloys and the size of the impact craters were measured employing special optical microscopy (OM) and scanning electron microscopy (SEM) techniques. The crater size and related damage were considered in terms of: (a) the microstructure and properties of the target, and (b) the impacting conditions, i.e. the particle, size, velocity and angle of impact. Throughout the investigation special attention was focused on the scaling between the crater size and the microstructure (e.g. the WC grain size).

A comparison of the results obtained for steady-state erosion produced by many impacts with those obtained in the present investigation on single impacts is the subject of a separate paper.

2. Experimental details

2.1. Target materials, microstructure and hardness

2.1.1. Materials

Cemented WC–Co alloys with binder contents ranging from 6 to 50 wt % (10.8 to 69.2 vol %) were employed as the target materials; the specific compositions

0022–2461/88 $03.00 + .12

TABLE I Microstructural parameters of the cemented carbide alloys (all dimensions are in μm; letters refer to the speciment identification codes)

Microstructure Parameters	6 wt % Co			10 wt % Co		15 wt % Co	20 wt % Co		50 wt % Co
	A	B	C	D	E	KS	LA	LB	GS
Intercept diameter (d_{WC})	0.57	1.10	3.25	0.49	1.40	2.23	0.63	1.84	0.42
Area (A_{WC})	0.35	1.12	8.65	0.34	1.84	5.7	0.50	3.35	0.54
Maximum diameter (d_{WC}^{max})	0.83	1.47	4.01	0.85	1.80	3.30	1.06	2.84	1.19
Shape factor (δ_{WC})*	0.79	0.79	0.77	0.70	0.80	0.76	0.67	0.63	0.68
Binder volume fraction (f_{Co})	0.108	0.108	0.106	0.163	0.163	0.236	0.306	0.306	0.692
Binder mean free path (λ_{Co})†	0.08	0.11	0.35	0.13	0.28	0.69	0.28	0.81	0.92
Binder mean free path (λ_{Co}^{C})‡	0.23	0.35	0.94	0.32	0.62	1.68	0.52	1.26	1.42
Contiguity (C)	0.65	0.69	0.63	0.59	0.55	0.59	0.46	0.36	0.35

*Shape factor $\delta_{WC} = 4\pi$ (area)/(perimeter)^2.
† λ_{Co} is the binder mean free path assuming the presence of a thin film of the binder between WC–WC interfaces, and is given by $\lambda_{Co} = d_{WC}f_{Co}/(1 - f_{Co})$.
‡ λ_{Co}^{C} is the binder mean free path assuming that there is no thin film of the binder between the contiguous WC–WC interfaces, and is given by $\lambda_{Co} = d_{WC}f_{Co}/[(1 - f_{Co})(1 - C)]$.

are given in Table I. The alloys containing 6 to 20 wt % binder were commercial alloys obtained from Kennametal Corporation, Greensburg, Pennsylvania; the alloy containing 50 wt % binder was obtained from Dr J Gurland of Brown University.

2.1.2. Microstructure

The microstructures of the alloys were established by sequentially polishing specimens from initial rough grinding with a 30 μm diamond-bonded disc to a final finish using 0.25 μm diamond paste and then etching with Murakami's etchant containing 10 g KOH and 10 g $K_3Fe(CN)_6$ in 100 ml H_2O, followed by a second etchant containing 4 ml HCl, 0.3 ml H_2O_2, 8 ml H_2O in 100 ml CH_5OH. The etched specimens were examined and photographed using SEM.

Microstructure size and shape parameters listed in Table I were determined from enlarged scanning electron micrographs (SEMs) using the following procedures. The binder volume fraction, f_{Co}, the binder mean free path, λ_{Co} or λ_{Co}^{C}, the mean linear intercept WC grain size d_{WC}, and the WC grain contiguity, C, were determined using the line-intercept method of Lee and Gurland [11]. The mean maximum WC grain diameter d_{WC}^{max}, the mean WC grain area, A_{WC}, and the mean WC grain shape factor, δ_{WC}, were determined from the SEMs using an Apple Graphics Tablet interfaced with an Apple II-plus computer and a special software package provided by Hare and Russ [12]. The outline of every WC grain in an enlarged SEM was traced with the graphic tablet's pen and the information fed into the computer, which recorded into sequential text files the perimeter, area, maximum diameter and shape factor for each WC grain. The data were subsequently recalled for statistical analysis using the software package.

The distributions of the parameters were in all cases approximately log-normal; their mean values are given in Table I.

2.1.3. Hardness

Vickers microhardness tests with loads of 100, 250 and 500 g were conducted on specimen surfaces prepared by grinding and polishing in the manner described above for the microstructure determinations. These loads produced impressions which were similar in size to the impact craters to be considered below. The average Vickers hardness, H_v, of about 10 tests on each specimen at each load are given in Table II. To be noted is that H_v decreases with increase in load. This is in accord with a more detailed study by Conrad, *et al.* [13] of the effect of applied load on the hardness of a WC–6 wt % Co alloy ($d_{WC} = 0.59\,\mu$m) in which the hardness decreased by 8% as the load was increased from 0.1 to 40 kg. Also worthy of mention, because it relates to the size of the impact craters to be discussed below, is that the number of WC grains encompassed by the projected area of the hardness impressions at the 100 to 500 g loads ranged between approximately 50 and 1000 for the materials considered here.

2.2. Impact conditions

Prior to impacting, the surfaces of the WC–Co alloy targets were ground and polished to a mirror finish using either 1 μm diamond paste (observation by OM) or 0.25 μm diamond paste (observation by SEM). They were then impacted with a small, controlled amount (0.025 g) of alumina particles at a fixed velocity, v (35 to 93 m sec^{-1}) and impact angle, α (30° to 90°) using an air-stream erosion system [14] with the paddle-wheel method [15] to calibrate the particle velocity. The number of particles employed was established by trial to give as large a

TABLE II Vickers hardness and projected area of the impression as a function of load, P

Specimen	f_{Co}	A_{WC} (μm^2)	P = 100 g		P = 250 g		P = 500 g	
			A_p* (μm^2)	H_v† (GPa)	A_p (μm^2)	H_v (GPa)	A_p (μm^2)	H_v (GPa)
A	0.11	0.35	45	20.15	120	18.92	251	18.07
B	0.11	1.12	55	16.49	144	15.73	287	15.79
C	0.11	8.65	65	13.97	187	12.15	3184	11.84
D	0.16	0.34	54	16.98	144	15.73	281	16.19
E	0.16	1.84	109	8.35	246	9.24	320	14.19
KS	0.24	5.70	72	12.61	181	12.57	430	10.55
LA	0.31	0.50	83	10.92	227	10.00	462	9.83
LB	0.31	3.35	100	9.05	254	8.95	450	10.09
GS	0.69	0.64	102	8.89	288	7.90	578	7.86
Co	1.0	-	364	2.49	970	2.34	2116	2.15

*A_p = projected area of hardness impression.
†H_v = static Vickers hardness.

number of craters as possible with only an occasional overlapping.

The alumina particles of grit sizes from 60 to 240 were purchased from the Norton Company. They were angular in shape (similar to those in [16]) and are estimated to have a Vickers hardness of ~ 20 GPa and a density of 3.9 g cm^{-3}. A detailed statistical analysis of the size and shape of the particles was performed [17] using a computerized image analysis [18] on photographs taken of a dispersion of the particles on a glass slide. The size distribution was approximately log-normal for each grit size. A summary of the results of the analysis of the size and shape of the particles is given in Table III. Unless stated otherwise, the particle size given in the remainder of the text will be the mean equivalent spherical diameter, D. The values of D for the grit sizes employed in this investigation ranged from 63 to 405 μm.

It was found that some fragmentation of the alumina particles occurred upon impact during steady-state erosion, the amount increasing with increase in particle size and velocity [14]. The amount of fragmentation was essentially nil at the velocities considered here for the 63 μm particles, but became as high as 19% for 270 μm particles impacting the surface at 93 m sec^{-1}.

2.3. Measurements on impact craters

Both OM and SEM were employed to determine the nature and geometry of the impact craters. OM was employed to obtain a statistical measure of the size (projected area onto the surface) of a large number of impact craters. Use of SEM at the low magnifications required for these statistical measurements was unsatisfactory due to a lack of contrast between the crater and the neighbouring surface. SEM was, however, used to determine the projected area and depth of some clearly defined craters (from which their volume and surface area were derived). Details regarding the two (OM and SEM) methods of measurement will now be given.

2.3.1. Optical microscopy (OM) measurements

Examples of the impact craters observed by optical microscopy (using polarized light and Zemarsky contrast) are given in Fig. 1. The size of each crater was determined from enlarged optical micrographs by tracing its perimeter using the Apple Graphics Tablet interfaced with the Apple II-Plus computer mentioned above, which recorded the perimeter, area and shape factor of the impression. About 150 to 200 craters were measured for each impact condition, care being taken to avoid overlapping craters. It was found that the average projected area, A_p, of the craters became fairly constant after about 25 to 50 measurements. Thus, the results based on the measurements of 150 to 200 craters were deemed to be representative of the overall population.

TABLE III Size and shape of the impacting alumina particles (all sizes are in μm and are mean values)

Grit no.	Mfg. (Norton) particle size, D*	D_p†	D_e‡	D_c§	D_s‖	Form factor ¶, δ_f	Elong. ratio**, E.R.
240	63	52 (± 14)	54 (± 15)	62	40 (± 19)	0.715 (± 0.102)	1.50 (± 0.29)
120	143	149 (± 43)	153 (± 45)	179	105 (± 46)	0.716 (± 0.108)	1.53 (± 0.32)
80	270	269 (± 40)	275 (± 32)	320	196 (± 82)	0.718 (± 0.093)	1.53 (± 0.33)
60	405	-	-	-	-	-	-

*D (equivalent spherical diameter): diameter of a sphere having the same volume as the particle.
†$D_p = (4A/\pi)^{1/2}$ (projected area diameter): diameter of a circle having the same area as the projected area A of the particle.
‡$D_e = (LB^2)^{1/3}$ (equivalent spherical diameter): diameter of the sphere having the same volume as the elipsoid whose major axis is the maximum Feret's diameter, L, and whose minor axis is the minimum Feret's diameter, B.
§D_c = Perimeter/π (perimeter diameter): diameter of a circle having the same perimeter as the projected outline of the particle.
‖D_s (sector diameter): length of an intercepted line of the projected particle.
¶$\delta_f = 4\pi A/(\text{perimeter})^2$ measures deviation from circular form, e.g. δ_f = 1.0 for circle, 0.785 for square and 0.605 for triangle.
**E.R. = L/B (elongation ratio).

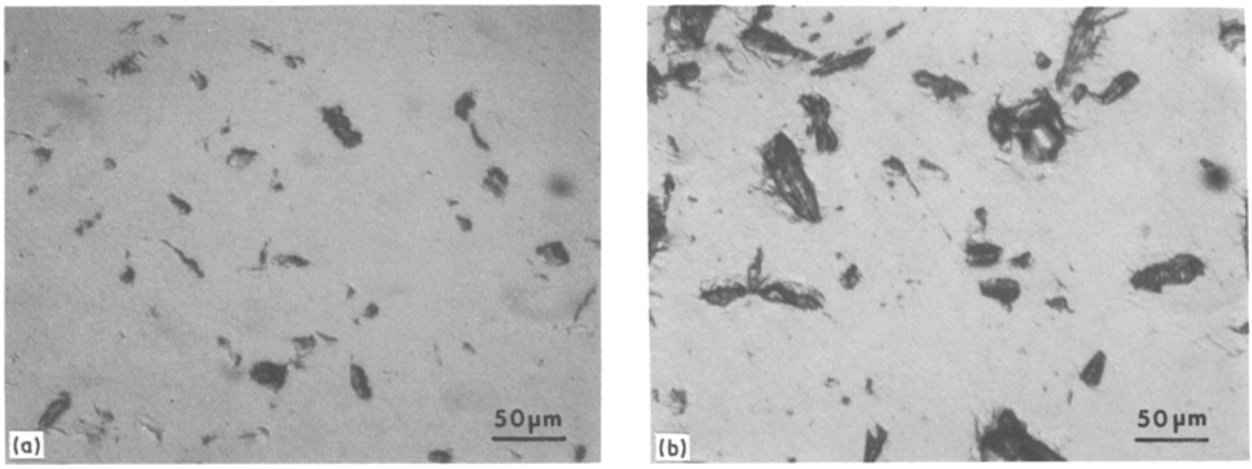

Figure 1 Optical micrographs of impact craters in the following materials: (a) WC–6 wt.% Co, $d_{WC} = 0.57\,\mu m$, and (b) pure cobalt. Impact conditions: $D = 270\,\mu m$, $v = 50\,m\,sec^{-1}$ and $\alpha = 90°$.

2.3.2. Scanning electron microscopy (SEM) measurements

The depths at various locations of a given crater were determined from SEMs taken at two tilt angles (0° and 20°) with respect to the electron beam [19]. The tilt axis was chosen such that the crater was displaced in the Z- and Y-direction (Fig. 2), but not in the X-direction. Upon tilting, the specimen moved in the Z-direction, thereby changing the working distance in the SEM and causing the image to become out of focus. Refocusing was accomplished by using the Z-control knob without changing the electron optics or the magnification. As the specimen stage was not eccentric, the image also moved in the Y-direction. The selected crater was then brought back into the field of view by translating the image in the Y-direction. The crater depth was determined by measuring the relative shifts of discernable features with respect to reference points far from the crater. The depth, h, was calculated using the following equation based on Fig. 2 [19]

$$h = (d_1 \cos \phi - d_2)/\sin \phi \qquad (1)$$

At least 50 to 60 different features were chosen within a crater and their respective depths determined. The data were stored in a microcomputer and computations made using the software developed by Russ and Hare [20] to yield the corresponding computer-generated contour map, the crater surface area and the crater volume. The contour maps indicated that the material displacement was in general not uniform, but rather contained localized regions of intense deformation. Measurements were made on about 25 craters for each test condition to obtain the average crater surface area, A_s, and volume, V. Further, the projected area, A_p, of each of the craters was determined from the SEMs using the graphics tablet. Reasonable accord ($\pm 10\%$) existed between the value of the projected area of a given crater determined by SEM and that by OM, providing confidence in the OM measurements.

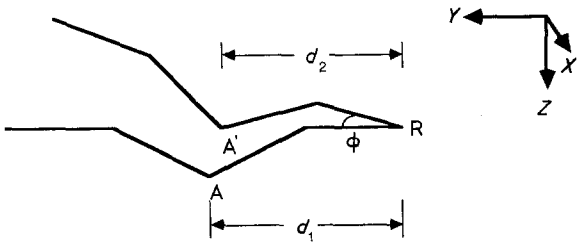

Figure 2 Geometry relating to the determination of the crater depth. d_1 is the distance between the reference point R some distance from the crater and a discernable feature A within the crater. d_2 is the distance of the same feature after a tilt of ϕ degrees. The Y- and Z-directions are in the plane of the paper, while the X-direction is normal to this plane. The reference point is chosen such that the line joining R and A is perpendicular to the XZ reference plane.

3. Results

3.1. Impact crater shape and size

3.1.1. Projected area (OM)

The projected areas of the craters had shape factors, δ_c, of 0.4 to 0.6, which were in general lower for the larger craters. They tended to be slightly elongated with an average aspect ratio of 1.25. The distribution of crater areas was strongly skewed towards the smaller sizes compared to the distribution of the impacting particle sizes; see Fig. 3. Plotted here are the normalized frequencies, f/f_{max}, for both (a) the normalized impact areas A_p/A_p^{max}, and (b) the normalized particle sizes, D/D_{max}, for impacts of 80 grit Al_2O_3 particles ($D_p = 125$ to $400\,\mu m$) on the WC–6 wt % Co alloy

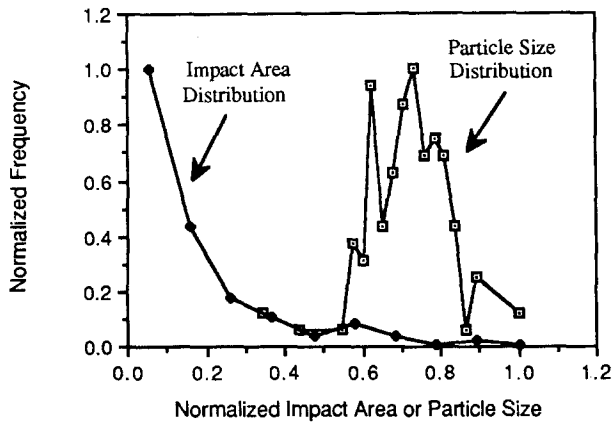

Figure 3 Comparison of the distribution of impact crater areas on specimen A ($f_{Co} = 0.11$, $A_{WC} = 0.35\,\mu m^2$) with the distribution of the impacting particle sizes for 80 grit alumina powder ($D = 270\,\mu m$). Impact conditions: $v = 50\,m\,sec^{-1}$, $\alpha = 90°$.

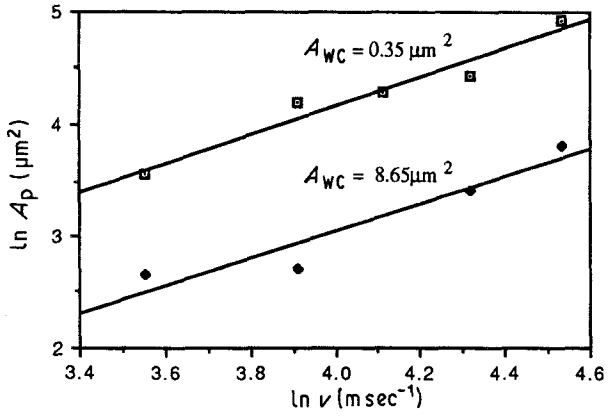

Figure 4 Log–log plots of mean projected impact area, A_p, against particle velocity v for two WC–6 wt % Co alloys representing extremes in WC grain size (A_{WC} = 0.35 and 8.65 μm^2). Impact conditions D = 143 μm, α = 90°.

with $A_{WC} = 0.35\,(mm)^2$. Evident in Fig. 3 is a wide distribution of impact areas, but having no direct correlation with the impacting particle size distrbution. To check further whether or not there existed any direct correlation between the distribution of crater areas and the impacting particle sizes, a further classification of the 80 grit particles was carried out employing a series of standard ASTM sieves to yield particles whose sieve sizes, D_{sieve}, now ranged between 210 and 246 μm compared to the sieve sizes of 98 to 246 μm of the original Al_2O_3 powder. No significant change in the impact crater area distribution resulted for this more restricted distribution of impacting particle sizes. It was therefore concluded that the size distribution of the impact craters for a given particle size resulted mainly from the variation in orientation of the impacting particles as they struck the surface and their subsequent response, which consisted of rotation and skidding of the particle at the surface, and possible fragmentation. In the discussion to follow, the mean value of the projected area, A_p, will be considered unless stated otherwise.

It was found that A_p increased with increase in particle size, D, and velocity, v, and with increase in cobalt-content; see Figs 4 to 6. A reasonable fit to a straight line is indicated in the log–log plot (Fig. 4) of A_p against v for the two WC–6 wt % Co alloys representing extremes in the WC grain size, yielding

$$A_p = \beta v^b \qquad (2)$$

with b = 5/4. β depends on the WC grain size (and presumably the cobalt content). In Fig. 5, A_p increases in a linear fashion with D. Extrapolation of the straight line to the abscissa gives D_0 = 50 μm as the limiting particle size which will produce an impact crater for the given test conditions. Taking the average linear size of the crater $d_p = A_p^{1/2}$, one obtains that the ratio $d_p/D \approx 0.04$ from the results in Fig. 5. In Fig. 6 it is seen that A_p increases in an approximately linear manner with the binder volume fraction.

The effect of WC grain size on A_p (Fig. 7) is not as straightforward as for the parameters considered above. It is here seen that A_p tends to go through a maximum at $A_{WC} \simeq 1.1\,\mu m^2$. As will become evident below, this behaviour results from the effect of scaling between the crater size and the WC grain size on the nature of the impact damage mechanism. An increase in A_p with increase in A_{WC} occurs when the scaling ratio A_p/A_{WC} is $\lesssim 50$, whereas the lower values of A_p at the largest WC grain size are associated with a scaling ratio < 10.

The effect of impact angle, α is shown in Fig. 8. In this case A_p goes through a maximum at α = 50°. It was found that the angle at which A_p was a maximum depended on the number of WC grains encompassed by the projected area of the crater, i.e. by the ratio A_p/A_{WC}. When A_p/A_{WC} was < 10, the maximum value of A_p occurred at α = 90°. As the ratio increased above 10, the angle at which the maximum in A_p occurred decreased becoming $\sim 45°$ when A_p/A_{WC} was > 200.

3.1.2. Projected area, surface area and volume (SEM)

The mean values of the actual crater surface are, A_s, and the crater volume, V, derived by computer analysis of the crater depth, h, measurements are given in Table IV; also included are the mean projected areas, A_p, determined from the SEMs. A plot of V against $A_p^{1.5}$ for individual craters on two alloys of nearly the same WC grain size but differing in cobalt content is presented in Fig. 9. The data fit a straight line through the origin, giving

$$V = \kappa A_p^{3/2} \qquad (3)$$

with κ = 0.069. The exponent 3/2 is in accord with expectations based on a simple geometric form.

Examples of the two extremes in the type of damage produced by the single particle impacts are given in

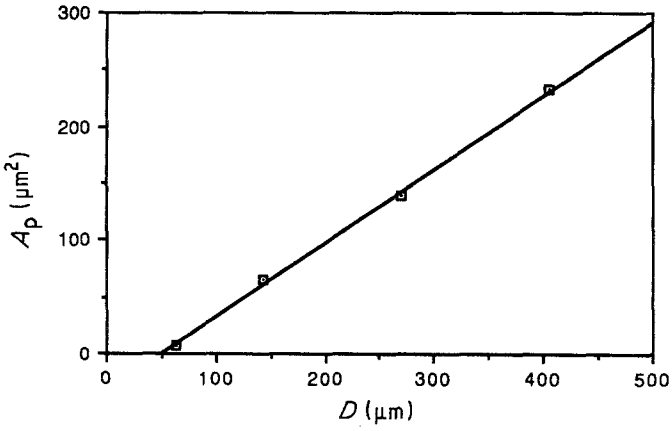

Figure 5 Mean projected impact are, A_p plotted against particle size D, for the WC–6 wt % Co alloy of intermediate WC grain size (A_{WC} = 1.1 μm^2). Impact conditions: v = 50 m sec^{-1}, α = 90°.

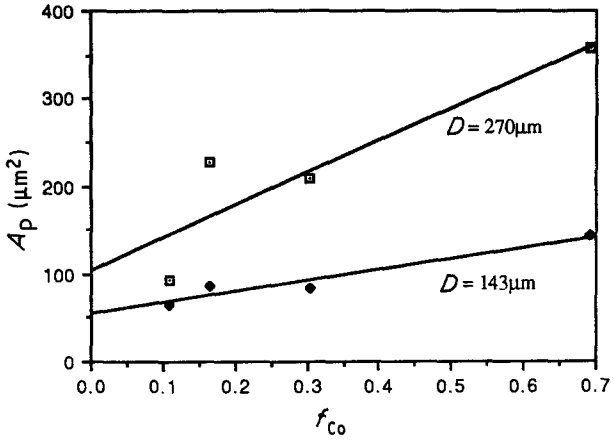

Figure 6 Variation of mean projected area, A_p, with cobalt content for the WC–Co alloys with $A_{WC} = 0.35$ to $0.50\,\mu m^2$. Impact conditions: $D = 143$ and $270\,\mu m$, $v = 50\,m\,sec^{-1}$, $\alpha = 90°$.

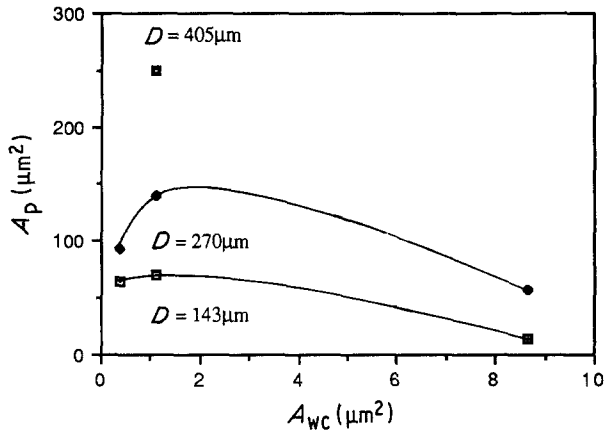

Figure 7 Mean projected impact area, A_p plotted against the mean WC grain area A_{WC} of the WC–6 wt % Co alloys as a function of the impact conditions, $v = 50\,m\,sec^{-1}$, $\alpha = 90°$.

Figs 10 and 11. The type of damage illustrated in Fig. 10 (here termed Type I) occurred when the impact crater encompassed only a few (at most 10) WC grains, i.e. $A_p/A_{WC} < 10$. Evident is cracking and crushing of the brittle WC grains. Debonding of the WC grains along their contiguous boundaries and at the cobalt matrix interface also occurred in some cases. These damage features (i.e. cracking, crushing and debonding) occurred very frequently at the WC grain edges and corners, similar to the situation in Fig. 10. The impact craters did not exhibit the usual features characteristic of cone cracks or lateral cracks, which are generally observed for the impact of single-phase brittle materials [9, 10].

Fig. 11 shows the type of damage (termed Type II) produced when the impact crater encompasses 100 or more WC grains, i.e. $A_p/A_{WC} > 100$. In this case the crater resembles that observed for the impact of ductile materials, being characterized by appreciable plastic deformation with the formation of ridges and lips at the crater edges. The plastic deformation has mainly occurred in the binder phase, the WC grains remaining relatively intact. The ductile character of the crater for the condition when $A_p/A_{WC} > 100$ was especially evident for oblique impact; see Fig. 12.

When the crater encompassed an intermediate number of WC grains (i.e. $\sim 10 < A_p/A_{WC} \lesssim 100$), the damage consisted of a mixture of Types I and II; see for example Fig. 13. The degree of the ductile-type damage features in such cases increased with the number of WC grains encompassed, i.e. with increase in the ratio A_p/A_{WC}.

The micrographs of Figs 10 to 13 are for impacts on 6 wt % Co alloys. Similar damage features and behaviour were noted for the alloys with higher cobalt contents. However, at intermediate values of A_p/A_{WC}, more cracking of the WC grains generally occurred as the cobalt content increased, especially near the edges of the crater; see for example Fig. 14. This increased cracking probably resulted from the fact that for given impact conditions the crater became deeper with increase in cobalt content, representing a larger amount of plastic deformation of the binder phase and in turn a greater stress on the WC grains.

4. Discussion

The results presented above indicate that the single-particle impact damage of WC–Co alloys can be classified into two principal regimes based on scaling between the crater size and the WC grain size: Regime I, where the crater encompasses less than about 10 WC grains and the damage is of a brittle type, and Regime II, where the crater encompasses more than about 100 WC grains and the damage is of a ductile type. Because the nature of the damage differs markedly in the two regimes, the discussion to follow will consider each regime separately.

4.1. Brittle behaviour (Regime I)

As mentioned above, the damage in this scaling regime consists mainly of the crushing and cracking of the WC grains, the appearance of the cracks differing from that normally associated with either cone or lateral cracks. The projected area of the crater in this regime increased with particle velocity (see specimen with $A_{WC} = 8.65\,\mu m^2$ in Fig. 4) and its maximum value as a function of impact angle occurred at $\alpha = 90°$. Taking the average linear dimension of the crater, d_p, equal to $A_p^{1/2}$ and inserting into Equation 2, one obtains

$$d_p \propto v^{5/8} \quad (4)$$

The value of the exponent in Equation 4 is smaller

TABLE IV Mean values of the projected area, A_p, the depth, h, actual surface area, A_s, and the volume, V, of impact craters determined by SEM for two WC–Co alloys. Impact conditions: $D = 270\,\mu m$, $v = 50\,m\,sec^{-1}$, $\alpha = 90°$

Specimen	f_{Co}	d_{WC} (μm)	A_{WC} (μm^2)	h (μm)	A_p (μm^2)	A_s (μm^2)	V (μm^3)	h/d_{WC}	A_p/A_{WC}
A	0.11	0.57	0.35	1.15	114	127	123	2.02	326
D	0.16	0.49	0.34	1.75	298	358	368	3.57	876

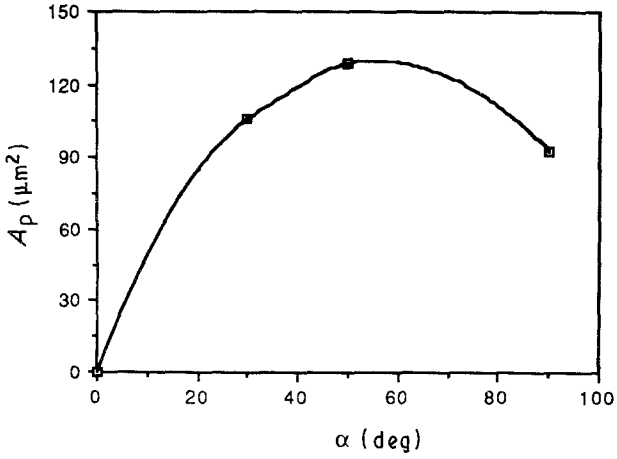

Figure 8 Mean projected impact area, A_p, plotted against impact angle α for the WC–6 wt % Co alloy with $A_{WC} = 0.35\,\mu m^2$. Impact conditions: $D = 270\,\mu m$, $v = 50\,m\,sec^{-1}$. Specimen A.

than that (4/5) predicted for the effect of particle velocity on the radius of a Hertzian cone crack [21, 22] or those (8/9 to 2) for the radial crack length in elastic-plastic indentation fracture of brittle materials [23–25].

4.2. Ductile behaviour (Regime II)

As the impact craters in this scaling regime resemble those for ductile materials, it seems reasonable to consider the results in terms of the impact of a massive ductile target by a rigid projectile. Providing that the projectible does not deform or fracture, and neglecting any elastic effects, one obtains [26–28]

$$pV = mv^2/2 \qquad (5)$$

where p is the pressure acting uniformily over the contact area, V the volume of the resulting crater, $m = (\pi D^3 \varrho/6)$ the mass of the impacting particle with density, ϱ, and whose velocity is v. In Equation 5 the kinetic energy, U, of the particle is equated to the work, W, involved in forming the crater. For the case where a significant fraction, f, of W is associated with plastic deformation, one can take p equal to the hardness, H_v. Further, since it was found in the present

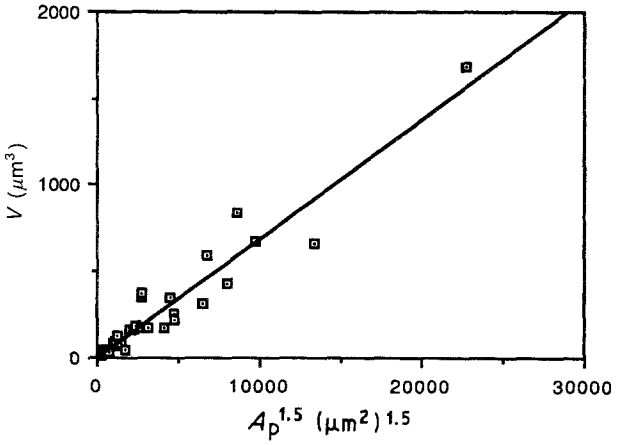

Figure 9 Crater volume, V, plotted against projected area, $A_p^{1.5}$ (both determined by SEM) for impact on two WC–Co alloys (6% and 10% wt Co) with $A_{WC} \approx 0.3\,\mu m^2$. Impact conditions: $D = 270\,\mu m$, $v = 50\,m\,sec^{-1}$, $\alpha = 90°$.

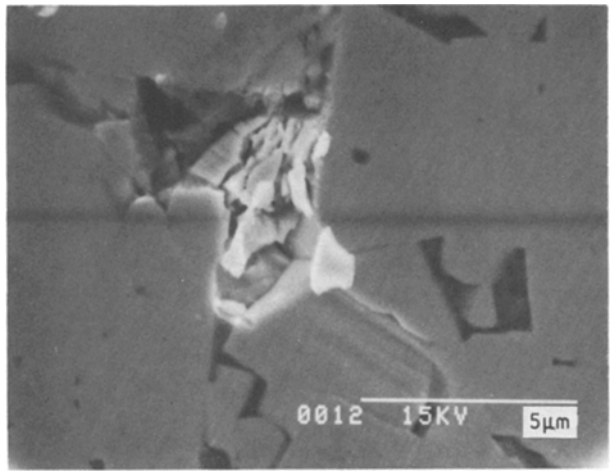

Figure 10 Nature of the impact damage in a WC–6 wt % Co alloy with $A_{WC} = 8.65\,\mu m^2$ when the projected area of the crater is of the order of the WC grain area. Impact conditions: $D = 63\,\mu m$, $v = 50\,m\,sec^{-1}$, $\alpha = 90°$.

study that $V = \kappa A_p^{3/2}$, Equation 5 yields

$$A_p = (f\pi\varrho D^3 v^2/12\kappa H_v)^{2/3} \qquad (6)$$

Hence, a log–log plot of A_p against the quantity (D^3v^2/H_v) should yield a straight line of slope 2/3. Such a plot is given in Fig. 15 for all the measurements of A_p (impact conditions: $D = 143$ and $270\,\mu m$, $v = 50$ and $93\,m\,sec^{-1}$, $\alpha = 90°$) and taking H_v equal to the Vickers hardness at the 250 g load. As shown in Fig. 15, at this load the projected areas of the hardness impressions $A_{p,v}$ are intermediate compared to those of the impact craters. Also to be noted is that the data points for the most part cluster about two parallel straight lines with slope 2/3. The results for $A_p/A_{WC} < 10$ lie on the lower line; while those for $A_p/A_{WC} > 100$ fall mainly on the upper line. In the latter case, those data points which fall below the upper line were generally obtained for the larger ($D = 270\,\mu m$) particles at the higher velocities.

Taking $\varrho = 3.9\,g\,cm^{-3}$ and $\kappa = 0.069$ (from Fig. 9), one obtains $f = 0.09$ for the upper straight line in Fig. 15 and $f = 0.01$ for the lower line. The low value

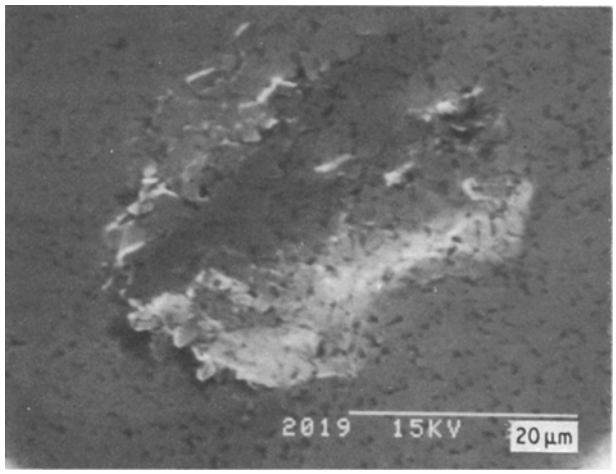

Figure 11 Nature of the impact damage in a WC–6 wt % Co alloy with $A_{WC} = 1.12\,\mu m^2$ when the projected area of the crater encompasses more than 100 WC grains. Impact conditions: $D = 405\,\mu m$, $v = 50\,m\,sec^{-1}$, $\alpha = 90°$.

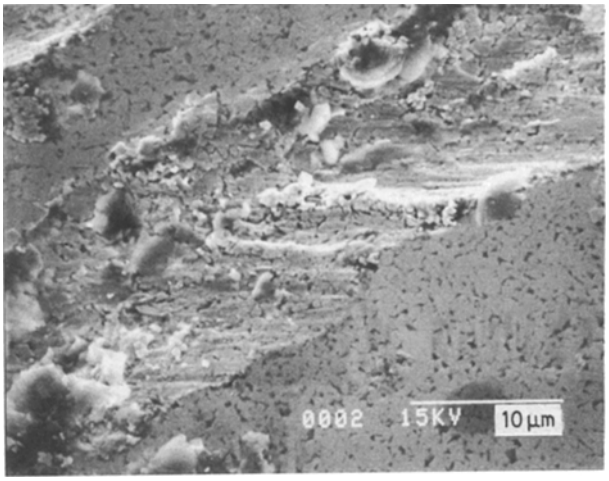

Figure 12 Nature of the damage for an oblique impact angle in a WC–6 wt % Co alloy with $A_{WC} = 0.35\,\mu m^2$ when the projected area of the crater encompasses more than 100 WC grains. Impact conditions: $D = 405\,\mu m$, $v = 50\,m\,sec^{-1}$, $\alpha = 40°$.

of f for the lower line was not surprising, because the data points giving this line are for impact conditions where brittle fracture of the WC grains was the dominant damage mechanism. Equation 6 was not expected to apply to this regime, and hence the fit of the data to a straight line of slope 2/3 may be fortuitous. The value of $f = 0.09$ obtained for the ductile-type crater is, however, smaller than expected for the impact of ductile targets by rigid projectiles, where it is generally assumed that $f \approx 0.9$ [27]. A 10% loss in kinetic energy is considered to result from three elastic phenomena: (a) kinetic energy of the rebounding particle (1 to 10% loss) [29–31], (b) elastic vibrations in the particle (a small amount) [27], and (c) the elastic wave field propagating into the target (1 to 5%) [27]. The kinetic energy of the rebounding particle may amount to somewhat more than the 1 to 10% loss indicated above, if an appreciable increase in its rotational velocity occurs following impact. For example, Hutchings [32] reported for the oblique impact of metals by square plates that the rotational energy after impact represented 5 to 20% of the initial kinetic energy. Hence, a liberal estimate of the energy loss due to all elastic phenomena could be as high as 7 to 35% of the initial kinetic energy.

Additional factors which could lead to a lower value of f in Equation 6 are: (a) fragmentation of the particles upon impact, (b) cracking and debonding of the WC grains and (c) an effect of strain rate on hardness. The magnitude of these factors will now be considered in the order in which they are listed. As mentioned above, fragmentation of the impacting particles was observed in steady-state erosion tests on WC–Co alloys [14], the degreee of fragmentation increasing with increase in particle size and velocity, becoming about 20% for 270 μm particles at a velocity of $93\,m\,sec^{-1}$. Also, in the study [14] of the influence of the impacting particle flux on the steady-state erosion of aluminium 1018 steel and WC–6 wt % Co alloys it appeared that fragmentation of the particles may have influenced their rebound characteristics. Further, the fact that the anomalously low values of A_p in Fig. 15 occurred for the larger particles and higher velocities suggests that fragmentation may have been a contributing factor.

Fragmentation of the impacting particles can lead to two modes of energy loss: (a) that due to the resulting increase in surface area of the fragmented particles and (b) that due to the kinetic energy of the scattered fragments. A rough estimate of the energy due to the increase in surface energy can be obtained if we assume that the particles are cubes before and after fracture and that their size distribution remains constant. Making these assumptions, it can be shown that the fraction of the initial kinetic energy, U, consumed in creating new surfaces due to cleavage is given by

$$f(\text{cleavage}) = \frac{\Delta A_s \gamma_s}{U} = \frac{12\,[(1 - a)/a]\gamma_s}{D\varrho v^2} \quad (7)$$

where ΔA_s is the increase in surface area by cleavage of a particle whose surface energy is γ_s and $a = D_i/D$ is the ratio of the average size, D_i, of a particle after impact to that, D, before. Taking the reasonable values $a = 0.9$, $\gamma_s = 2000\,erg\,cm^{-2}$, $D = 143\,\mu m$ and $v = 50\,m\,sec^{-1}$, we obtain f (cleavage) = 0.002, which is insignificant. If fragmentation occurs by crushing [33, 34] rather than simple cleavage, a significantly

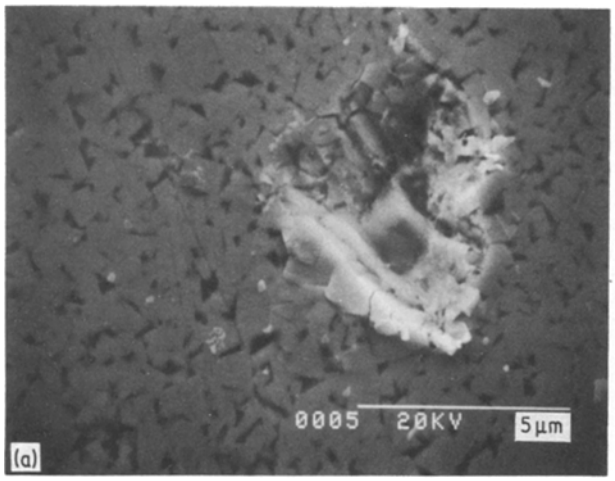

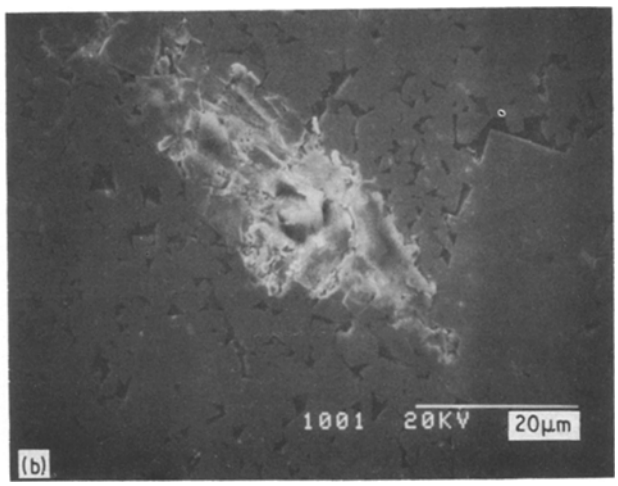

Figure 13 Nature of the impact damage in WC–6 wt % Co alloys when the projected area of the crater encompasses between 10 and 100 WC grains. (a) $A_{WC} = 0.35\,\mu m^2$, $D = 63\,\mu m$, $v = 75\,m\,sec^{-1}$, $\alpha = 90°$ and (b) $A_{WC} = 8.65\,\mu m^2$, $D = 270\,\mu m$, $v = 93\,m\,sec^{-1}$, $\alpha = 90°$

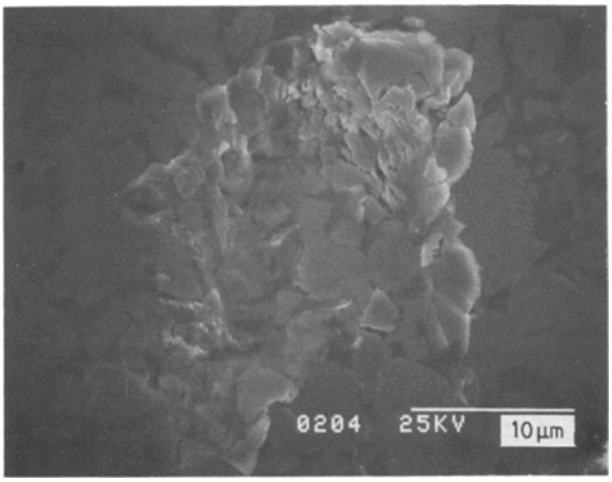

Figure 14 Nature of the impact damage in a WC–20 wt % Co alloy with $A_{WC} = 3.3\,\mu m^2$ and the ratio $A_p/A_{WC} = 30$. Note cracking of the WC grains near the edge of the crater. Impact conditions: $D = 270\,\mu m$, $v = 50\,m\,sec^{-1}$ and $\alpha = 90°$.

larger increase in surface area would occur and in turn the value of f might conceivably reach 2% or more.

It has been observed [33–35] that when a particle fragments upon impact there occurs a stream of fine debris which radiates from the impact site at velocities ranging from 0.3 to 4 times the initial particle velocity. It is easily shown that the ratio of the kinetic energy of the stream of fragments, U_{frag}, to the initial kinetic energy, U, is given by

$$U_{frag}/U = (1 - a^3)b^2 \quad (8)$$

where $a = D_i/D$ defined above $b = v_{frag}/v$ is the ratio of the velocity of the fragments, v_{frag}, to the initial particle velocity, v. Taking $a = 0.9$ and $b = 1$, we obtain $U_{frag}/U = 0.27$, which amounts to a significant energy loss. Appreciably higher or lower values for this energy loss ratio can result, depending on the values of a and b.

Turning our attention to the target, some energy loss in addition to that associated with plastic deformation can occur as a result of the cracking and debonding of the WC grains. The magnitude of this loss is expected to be small (at most 1%), in view of the small amounts of cracking and bonding actually observed in the ductile regime.

The value of the hardness employed in Equation 6 is the static hardness obtained at a plastic rate of about $10^{-2}\,sec^{-1}$. In impact tests of the type considered here the strain rate is estimated to be 10^5 to $10^7\,sec^{-1}$ [36–38]. The dynamic hardness of metals at these high strain rates has been found to be higher by 10 to 100% over the static hardness [38-41]. An estimate of the increase in the hardness of the WC–Co alloys which occurs as a result of the increased strain rate upon impact can be made based on data by Schenck *et al.* [42] on the effect of strain rate, $\dot{\varepsilon}$ on the flow stress, σ of WC–6 wt % Co alloys. They found for their alloys that the activation volume V^*, given by

$$V^* = 2kT\,(\partial \ln \dot{\varepsilon}/\partial\sigma) \quad (9)$$

was relatively constant at high stresses, being $\sim 10^{-21}\,cm^3$. k is Boltzmann's constant T the absolute temperature. Rearranging Equation 9 and taking $H_v = 3\sigma$ [26, 27], one obtains

$$\Delta H_v = 3\Delta\sigma = \frac{2kT \ln (\dot{\varepsilon}_i/\dot{\varepsilon}_s)}{V^*} \quad (10)$$

where $\dot{\varepsilon}_i$ is the plastic strain rate at impact and $\dot{\varepsilon}_s$ that during a static hardness test. Taking $T = 300\,K$, $\dot{\varepsilon}_i = 10^6\,sec^{-1}$, $\dot{\varepsilon}_s = 10^{-2}\,sec^{-1}$ and $V^* = 10^{-21}\,cm^3$, we obtain $\Delta H_v = 3.1\,GPa$ for the increase in hardness of

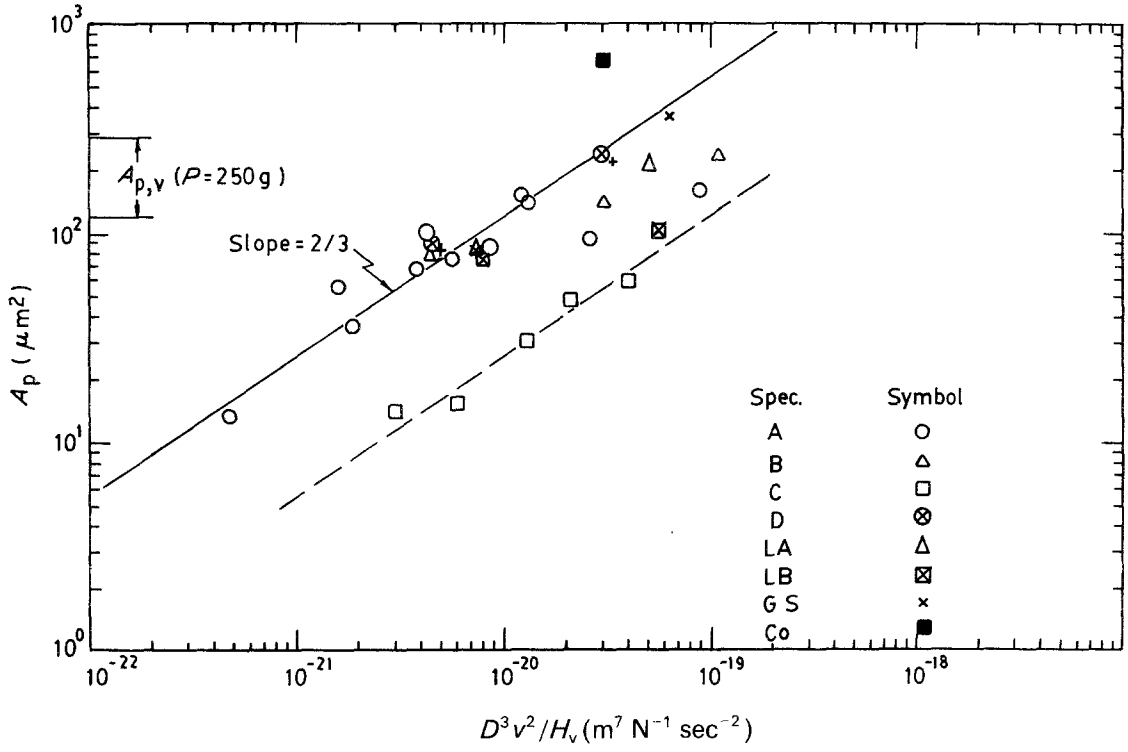

Figure 15 Log–log plot of A_p against the parameter D^3v^2/H_v, for WC–Co. Impact conditions: $D = 143$ and $270\,\mu m$, $v = 50$ and $93\,m\,sec^{-1}$, $\alpha = 90°$.

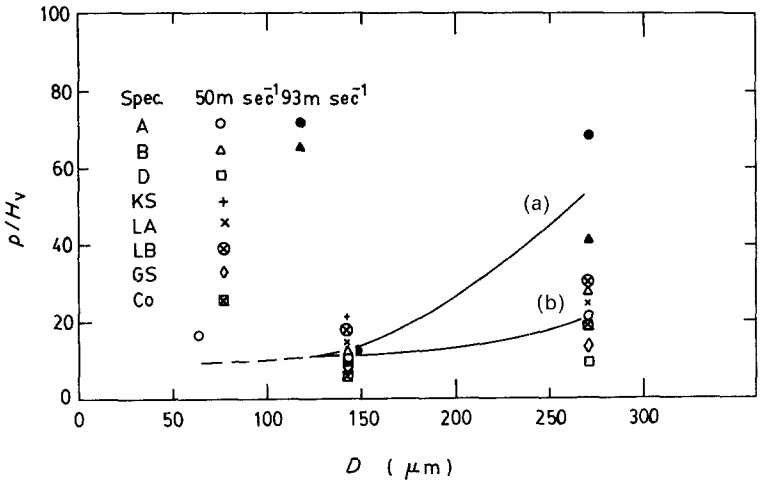

Figure 16 The ratio of p/H_v plotted against the initial particle size, D, as a function of initial velocity, v for the dutile regime, for WC–Co, $A_p/A_{WC} > 100$, $\alpha = 90°$; (a) $v = 50\,m\,sec^{-1}$, (b) $v = 93\,m\,sec^{-1}$.

the WC–Co alloys due to the increased strain rate at impact. This increase in hardness leads to an increase in f of Equation 6 from 0.09 to 0.10–0.12 depending on the static hardness.

Based on the above considerations, we have made estimates of the fraction of the initial kinetic energy consumed by the various processes which occur during impact; these estimates are given in Table V. The fact that the sum of the fractions amounts to 0.62 rather than unity suggests that we may have underestimated the energy consumed by one or more of the processes. The value of 0.62, is however, sufficiently high to support Equation 6 as a reasonable description for the formation of the ductile-type craters in WC–Co alloys.

Another approach to evaluating the experimental results is to compare the derived value of the dynamic flow pressure, p, with the measured static Vickers hardness, H_v, similar to Rickerby and Macmillan [28, 38]. The values of p were therefore calculated from Equation 5 by taking $V = 0.069\,A_p^{3/2}$. The ratio p/H_v obtained thereby is plotted against the initial particle size, D, at two initial velocities, v, in Fig. 16. The individual data points for a given D each represent a separate alloy. To be noted is that the ratio p/H_v increases with D and v over the range considered. No clear effect of WC grain size or cobalt content on p/H_v could be ascertained within the scatter of the data. The value of p/H_v at $D = 143\,\mu m$ is ~ 11, which is in accord with $f = 0.09$ ($\sim H_v/p$) derived from Fig. 15, indicating consistency in the analyses. The marked increase in the ratio p/H_v with D and v supports the idea proposed above that a significant fraction of the initial kinetic energy of the particle may be consumed in its fragmentation. Worthy of mention is that the value of 11 for the ratio p/H_v obtained here for the impact of WC–Co alloys by small angular particles is somewhat higher than the values of 1 to 5 obtained by Rickerby and Macmillan [28, 38] for the impact of aluminium, nickel, MgO and LiF single crystals and aluminium polycrystals by spherical steel and WC–6 wt % Co particles of $\sim 1.58\,\mu m$ diameter, for which no fragmentation was indicated.

Finally, of interest is the effect of target microstructure on the hardness of Wc–Co alloys were above analysis leads to the conclusion that the major effect of the microstructure on the crater size is through its influence on the hardness H_v in Equation 6. Therefore, three correlations of the effects of microstructure on the hardness of Wc–Co alloys were considered: (a) that of Lee and Gurland [11], (b) that of Chermant and Osterstock [43] and (c) that of Laugier [44]. Appropriate plots were made to check each of these correlations for the three hardness test loads employed here and the correlation coefficient of the best fit line for each relation was determined. The correlation coefficient (CC) ranged between 0.76 to 0.96 (see Table VI), increasing with increase in test load and by taking the contiguity $C = 0$ rather than the measured value given in Table I. The best correlation at all three test loads was for the Lee and Gurland [11] relation, which gave a CC of 0.88 for the 100 g load and 0.96 for the 500 g load assuming $C = 0$. Only slightly lower values of the CC (0.87 to 0.95) were obtained by taking the contiguity, C, equal to those listed in Table I. Thus, a reasonable description of the effect of microstructure on the impact crater size is obtained by substituting the Lee and Gurland [11] relation for H_v in Equation 6.

TABLE V Estimate of the fractions of the initial kinetic energy consumed by the various processes which occur during impact of the WC–Co alloys in the ductile regime

Process	Fraction of initial kinetic energy
Dynamic plastic deformation	0.11
Cracking and debonding of WC grains	0.01
Elastic phenomena	0.20
Fragmentation of particles	0.30
Total sum	0.62

5. Conclusion

The following is a summary of the results obtained in this investigation and the conclusions derived.

1. In general, the size of the impact crater increased with impacting particle size and velocity and with the cobalt content of the target.

2. Two distinct types of behaviour occurred, depending on the number of WC grains encompassed by the projected area of the crater. When the number of WC grains encompassed was < 10, the crater formed mainly by the cracking of WC grains; when

TABLE VI Correlation of measured static hardness values of the WC–Co alloys with predictions

Reference	Equation	Contiguity, C	Correlation Coefficient (Vickers Hardness Test Load)		
			100 g	250 g	500 g
Lee and Gurland [11]	$H_v = H_{WC} f_{WC} + H_{Co}(1 - f_{WC} C)$*	Measured†	0.87	0.90	0.95
		0	0.88	0.92	0.96
Chermant and Osterstock [43]	$H_v = A\lambda_{Co}^{-1/2}$	Measured	0.79	0.81	0.90
		0	0.87	0.89	0.95
Laugier [44]	$H_v = A\lambda_{Co}^{-1/5}$	Measured	0.76	0.78	0.88
		0	0.85	0.87	0.94

*$H_{WC} = 1382 + 23.1\ d_{WC}^{-1/2}$ (kg mm^{-2}). $H_{Co} = 304 + 12.7\ \lambda_{Co}^{-1/2}$ (kg mm^{-2}).
†Given in Table I.

the number was > 100 the crater resulted mainly from the plastic deformation of the binder.

3. The detailed mechanism of the cracking of the WC grains in the brittle regime was not clear; the cracks did not have the features normally associated with either simple cone cracks or lateral cracks.

4. The results for the ductile regime correlated reasonably well with the model for plastic indentation. However, the calculated energy consumed in the plastic deformation amounted to only about 10% of the initial kinetic energy of the impacting particle.

5. Besides the usual elastic effects, fragmentation of the impacting particles was concluded to represent a significant fraction of the energy loss, especially for the larger particles and higher velocities.

6. The effects of microstructure of the target on the crater size in the ductile regime was deduced to be mainly through its effect on the hardness, which was found to be given reasonably well by the Lee and Gurland relation.

Acknowledgements

The authors gratefully acknowledge the support of this research by the US Department of Energy under grant DE-FG05-84ER45115. They also wish to thank Dr Y Shin for his assistance in the design and construction of the air-stream erosion tester and for many helpful discussions during the course of this investigation.

References

1. A. A. DANKIN, *Poroshkovaya Metallurgia* **94** (1970) 73.
2. KH. UNEMYAS, L. KLEISS, V. TUMANOV and J. TILDERMAN, *Poroshkovaya* **98** (1974) 135.
3. H. CONRAD, D. McCABE and G. A. SARGENT, 1st International Conference on Science of Hard Materials, edited by R. K. Vishanadham, D. F. Rowcliffe and J. Gurland (Plenum, New York, 1983) p. 175.
4. H. CONRAD, Y. W. SHIN and G. A. SARGENT, "Specialty Steels and Hard Metals", edited by N. R. Cousins and J. B. Clark (Pergamon, New York, 1983) p. 423.
5. K. ANAND, C. MORRISON, R. O. SCATTERGOOD, H. CONRAD, J. L. ROUTBORT and R. WARREN, 2nd International Conference on Science of Hard Materials, edited by E. A. Almond, C. A. Brookes and R. Warren, Institute of Physics Conference Series No. 75 (Adam Hilger, Boston 1986) p. 949.
6. G. L. SHELDON and I. FINNIE, *Trans. ASME J. Eng. Ind.* **88** (1966) 387.
7. S. K. HOVIS, J. E. TALIA and R. O. SCATTERGOOD, *Wear* **108** (1986) 139.
8. Y. W. SHIN, G. A. SARGENT and H. CONRAD, *Met. Trans. A* **18A** (1987) 437.
9. H. CONRAD, "Erosion of Ceramics", 3rd Berkeley Conference on Corrosion–Erosion–Wear of Materials at Elevated Temperatures, 29 to 31 January 1986, edited by A. Levy, (N.A.C.E., Houston, Texas, 1987) p. 77.
10. *Idem*, "Theories of Erosion for Ductile and Brittle Materials", presented at International Conference on Metallurgical Coatings, San Diego, California, (20 to 24, April 1987).
11. H. C. LEE and J. GURLAND, *Mater. Sci. Eng.* **33** (1978) 125.
12. T. HARE and J. C. RUSS, North Carolina State University, personal communication (1985).
13. H. CONRAD, Y. SHIN, W. CAO, unpublished results, North Carolina State University (1985).
14. K. ANAND, S. K. HOVIS, H. CONRAD and R. O. SCATTERGOOD, *Wear* **118** (1987) 243.
15. S. K. HOVIS, K. ANAND, H. CONRAD and R. O. SCATTERGOOD, *ibid.* **101** 69 (1985).
16. G. A. SARGENT, P. K. MEHROTRA and H. CONRAD, "Erosion: Prevention and Useful Applications", ASTM STP664, edited by W. F. Adler (American Society for Testing and Materials, Philadelphia, PA, 1979) p. 77.
17. Y. SHIN and H. CONRAD, in Progress Report DOE-ER-45115-1, "Microstructure Effects in Solid Particle Erosion", by H. Conrad and R. Scattergood for the period 1 January 1984 to 1 January 1985, p. 123.
18. JOHN C. RUSS and J. CHRISTIAN RUSS, *J. Microscopy* **135** (1984) 89.
19. JOHN C. RUSS, "Practical Stereology" (North Carolina State University 1986).
20. J. C. RUSS and T. HARE, *J. Microscopy*, in press.
21. P. K. MEHROTRA, G. A. SARGENT and H. CONRAD, "Corrosion–Erosion Behaviour of Materials", edited by K. Natesan (TMS–AIME, Warrendale, Pennsylvania, 1980) p. 1217.
22. G. A. SARGENT, P. K. MEHROTRA and H. CONRAD, in "Proceedings 5th International Conference on Erosion by Solid and Liquid Impact, (Cambridge University, Cambridge, 1979) p. 28-1.
23. A. G. EVANS, M. E. GULDEN and M. ROSENBLATT, *Proc. Roy. Soc. London* **A361** (1978) 343.
24. S. M. WIEDERHORN and B. R. LAWN, *J. Amer. Ceram. Soc.* **62** (1979) 66.
25. A. W. RUFF and S. M. WIEDERHORN, "Treatise on Materials Science and Technology", Vol. 16, edited by C. M. Preece (Academic, New York, 1979) p. 69.
26. D. TABOR, "The Hardness of Metals" (Clarendon, Oxford, 1951).
27. I. M. HUTCHINGS, in Proceedings 5th International Conference on Erosion by Solid and Liquid Impact, (Cambridge University, 1979) p. 36–1.
28. D. G. RIBCKERBY and N. H. MACMILLAN, *ibid.*, p. 29–1.
29. G. G. GRANT, R. BELL and W. TABAKOFF, University Cincinnati, Department of Aerospace Engineering, Rept. 73-36 (1973).

30. E. RAACK, *Wear* **13** (1969) 301.
31. W. J. HEAD and M. E. HARR, *ibid.* **15** (1970) 1.
32. I. M. HUTCHINGS, *Int. J. Mech. Sci.* **19** (1977) 45.
33. J. E. GOODWIN, W. SAGE and G. P. TILLY, *Proc. Inst. Mech. Eng. (London)* **184** (1969–70) 279.
34. G. P. TILLY and W. SAGE, *Wear* **16** (1970) 447.
35. H. UUEMOIS and I. KLEIS, *ibid.* **31** (1975) 359.
36. R. E. WINTER and I. M. HUTCHINGS *ibid.* **29** (1974) 181.
37. I. M. HUTCHINGS, Proceedings of the Conference on Corrosion/Erosion Coal Conversion System Materials, (N.A.C.E., Houston, Texas, 1979) p. 393.
38. D. G. RICKERBY and N. H. MACMILLAN, *Wear* **60** (1980) 369.
39. C. H. MOK and J. DUFFY, *Int. J. Mech Sci.* **7** (1965) 355.
40. I. M. HUTCHINGS, *Wear* **70** (1981) 269.
41. C. J. FAIRBANKS, R. S. POLVANI, S. M. WIEDERHORN, B. J. HOCKEY and B. R. LAWN, *J. Mater. Sci. Lett.* **1** (1982) 391.
42. S. R. SCHENCK, R. J. GLOTTSCHALL and W. S. WILLIAMS, *Mater. Sci. Engng* **32** (1978) 229.
43. J. L. CHERMANT and F. OSTERSTOCK, *Powder Met. Int.* **11** (1979) 106.
44. M. T. LAUGIER, *Acta Metall.* **33** (1985) 2093.

Received 7 September
and accepted 10 December 1987